

In response to Akutsu-sensei's comments on 2025-07-13

Email (Coleman-only): <https://mail.google.com/mail/u/1/#inbox/>

1 MTSCCleav: a Multivariate Time Series
2 Classification (MTSC)-based method for
3 predicting human Dicer cleavage sites

4 First Author^{1,2*}, Second Author^{2,3†} and Third Author^{1,2†}

5 ¹*Department, Organization, Street, City, 100190, State, Country.

6 ²Department, Organization, Street, City, 10587, State, Country.

7 ³Department, Organization, Street, City, 610101, State, Country.

8 *Corresponding author(s). E-mail(s): iauthor@gmail.com;

9 Contributing authors: iiauthor@gmail.com; iiiauthor@gmail.com;

10 †These authors contributed equally to this work.

11 **Abstract**

12 **Background:** MicroRNAs (miRNAs) are small non-coding RNAs (ncRNAs)
13 that regulate gene expression at the post-transcriptional level, thereby playing
14 essential roles in diverse biological processes. The biogenesis of miRNAs requires
15 dicer to cleave at specific sites on the precursor miRNAs (pre-miRNAs). Several
16 machine learning approaches have been proposed to predict whether an input
17 sequence contains a cleavage site. However, they rely heavily on complex feature
18 engineering or opaque deep neural networks. It results in a lack of generalizability
19 and a long running time. There is a need for an alternative modeling paradigm
20 that is accurate, fast, and simple.

21 **Results:** We proposed a novel approach to frame the task as a multivariate time
22 series classification problem. Various encoding methods have been proposed to
23 convert the sequence and the predicted secondary structure into a time series.
24 We also leveraged the probabilities of the base pairs in the predicted secondary
25 structure. Computational experiments demonstrate that our proposed method
26 can achieve better or comparable results using a simpler, more intuitive model
27 and less computational time. It achieves $3.7X \sim 28.8X$ speedup. Through per-
28 turbation experiments, we found that regions close to the center of pre-miRNAs
29 are essential for predicting human dicer cleavage sites.

30 **Conclusion:** By transforming the RNA sequence and its secondary structure
31 information into a time series and utilizing simple, state-of-the-art time series
32 classifiers, we achieved comparable or even superior performance in a simpler

33 and faster manner. Code is available at: <https://github.com/cyuab/time-series-classification-cleavage>.
34

35 **Keywords:** miRNA, Dicer Cleavage Site, Genomic signal processing (GSP),
36 (Multivariate) time Series Classification (MTSC, TSC)

37 1 Background

38 One of the most important theories in molecular biology is the central dogma. It
39 depicts the flow of genetic information [1, 2]. Proteins are the functional units. And
40 the information stored in DNA is used to create them. Genes (segments) in DNA are
41 used as templates for messenger RNAs (mRNAs) synthesis. An mRNA acts as a set
42 of instructions to assemble a chain of amino acids, which form a linear polypeptide.
43 To become biologically active, this chain is folded into a specific 3D structure, a
44 proper configuration that enables it to perform its desired functions. And this folded
45 polypeptide is called a functional protein, or simply a protein. This entire process
46 closely resembles how a computer program runs on a machine. The source code does
47 not function by itself. First, it is translated into assembly code (a lower-level, less
48 human-readable form) and then into an executable file that can actually perform the
49 intended tasks [3].

50 These mRNAs are called “coding RNAs” because they code for proteins. There are
51 other genes in which the final product is the RNA molecule itself. They are called non-
52 coding RNAs (ncRNAs). Two types of small ncRNAs are particularly important. They
53 are microRNAs (miRNAs) and small interfering RNAs (siRNAs). Their discovery was
54 recognized with the 2006 Nobel Prize in Physiology or Medicine¹, awarded for work
55 completed only eight years prior [1].

56 In this study, we focus on miRNAs. An miRNA can regulate the expression of
57 several proteins. Hence, understanding the biogenesis of miRNAs is of great value. It
58 involves the processing of primary miRNAs (pri-miRNAs). RNAs are 3D molecules.
59 However, it is hard to measure the 3D structure (tertiary structure) from the exper-
60 iment and predict it from 1D sequence. We can understand their properties by
61 analyzing their 1D sequence or 2D structure, known as secondary structure. RNA
62 sequence is easily obtained through sequencing. The sequence and its predicted
63 secondary structure of a pri-miRNA “hsa-let-7a-1” is shown in Fig. 1.

64 Recall that a pri-miRNA contains a hairpin loop, also called a stem loop. A
65 microprocessor complex comprising Drosa and DCR8 cleaves the pri-miRNA to
66 form a precursor miRNA (pre-miRNA) inside the nucleus. The stem-loop is still pre-
67 served, but the two arms become shorter. After that, the pri-miRNA is transported
68 by Exportin 5 from the nucleus to the cytoplasm. It is further cleaved by an enzyme
69 called dicer [4]. Dicer cleaves the stem-loop from the two arms at the two cleavage

¹The Nobel Prize in Physiology or Medicine 2006 - NobelPrize.org:

<https://www.nobelprize.org/prizes/medicine/2006/summary/> (Accessed on: 2025-06-13).

²Its miRBase entry: <https://mirbase.org/hairpin/MI0000060>. (Accessed on: 2025-06-12).

³RNAfold web server: <http://rna.tbi.univie.ac.at/cgi-bin/RNAWebSuite/RFNAfold.cgi>. (Accessed on: 2025-06-12). The figure is viewed in “forna”. This view option can be chosen on the website.

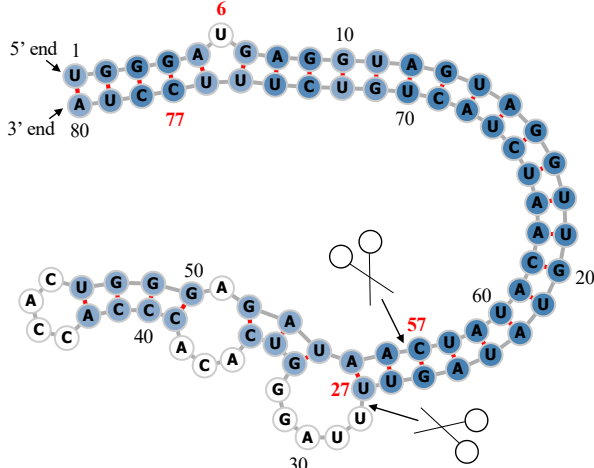


Fig. 1: Predicted secondary structure of the sequence S of pri-miRNA “hsa-let-7a-1”². Experimental evidence suggests that the two deviated mature miRNAs are $UGA \cdots GUU$ and $CUA \cdots UUC$. They are $S(6 : 27)$ and $S(57 : 77)$ (Both ends are inclusive.). The ends are highlighted in **bold**. Since $S(6 : 27)$ ($S(57 : 77)$) is near the 5' (3') end, we call it “5p (3p) mature miRNA”. The two scissors indicate the two cleavage sites. The color intensity of the nodes reflects their base pair probability in this predicted secondary structure. The deeper the color, the higher the probability. The unpaired nodes are uncolored. The raw figure is generated by RNAfold web server³.

70 sites, shown as the two scissors in Fig. 1. The stem-loop is removed. It results in a short
 71 double-stranded miRNA molecule, known as **an miRNA** duplex, which consists of the
 72 5p strand and the 3p strand⁴. These molecules may be subjected to additional trim-
 73 ming. The miRNA duplex is loaded into an RNA-induced silencing complex (RISC).
 74 RISC unwinds the duplex and tends to retain the strand with the less stable 5' end as
 75 the guide strand. The other strand is called the passenger strand. The retained strand
 76 guides the RISC to silence the target mRNA. Note that both strands can become the
 77 guide strand.

78 Dicer plays an important role in the biogenesis of miRNAs. It is reasonable to
 79 argue that the structure of the pre-miRNAs informs dicer about the cleavage pro-
 80 cess. It would be of great benefit to understand how dicer selects cleavage sites from
 81 the neighborhood information near the cleavage sites. Studies [5–7] revealed that the
 82 secondary structures are essential for cleavage site determination. Hence, to predict
 83 or classify whether a subsequence, extracted from the sequence of a pri-miRNA, con-
 84 tains a cleavage site, we can make use of both the sequence and secondary structure
 85 information. PHDcleav employed support vector machines (SVM), leveraging sequence
 86 and structure-based features [8] for the classification. LBSIZEcleav improved upon

⁴The 5p strand comes from the 5' arm while the 3p strand comes from the 3' arm. For the directionality, the 5p (3p) strand retains the original 5' (3') end of the pre-miRNA.

87 it by considering the loop and bulge lengths [9]. [10] proposed an ensemble learning
88 approach, using a gradient boosting machine for better accuracy. [11] developed
89 a deep learning model, namely DiCleave. This model used an autoencoder to learn
90 the secondary structure embeddings of pre-miRNAs from all the species in the miR-
91 Base database and leveraged this information. All these methods begin with curated
92 pre-miRNA sequences from the miRBase database. Their secondary structures are pre-
93 dicted. Patterns are extracted from the sequence and the secondary structure. They
94 create the positive cleavage patterns by setting the cleavage sites at the middle of the
95 patterns. The follow-up work of [11], which created the cleavage pattern by allow-
96 ing cleavage sites to appear at any position within the pattern, instead of the middle
97 only [12]. It created a much larger dataset. This increased dataset facilitates the learn-
98 ing of the deep learning method at the cost of increased running time. We utilized
99 the original dataset setting [8–11]. DiCleave is the current state-of-the-art (SOTA) for
100 this problem with the original dataset setting.

101 These models suffer several limitations. They rely heavily on complicated feature
102 engineering or opaque deep learning models [10–12]. It results in a lack of generaliz-
103 ability and a long running time. There is a need to design a simpler model so that it
104 can be easily extended to other prediction tasks on RNA data. One way to analyze
105 sequence data is to transform it into time series data. In response to this, we proposed
106 a multivariate time series classification-based method. Our contributions are shown as
107 follows.

- 108 1. To the best of our knowledge, we are the first to frame the prediction of the cleavage
109 sites as a multivariate time series classification problem.
- 110 2. We introduced several encoding methods to convert RNA data to time series.
- 111 3. We proposed utilizing the base-pair probabilities in the predicted secondary struc-
112 ture for the prediction. To our surprise, this information has been ignored in the
113 existing works.
- 114 4. We conducted perturbation-based experiments. It shows that regions close to the
115 cleavage sites are important for this problem. It agrees with the existing study [10].

116 2 Methods

117 The overall pipeline of this study is summarized in Fig. 2.

118 2.1 Data Preparation

119 We used miRBase database [13]⁵. The database comprises miRNA data from various
120 organisms [14]. The database contains 38589 miRNA records. Each record refers to
121 **an miRNA** sequence, along with other properties such as name, accession, organism,
122 and information on its derivative miRNA products. We are interested in pri-miRNA
123 in humans. The derivative miRNA products are the mature miRNAs. The database
124 also annotates the location of the mature miRNA within the original sequence and
125 indicates whether its existence has experimental evidence.

⁵The website is www.mirbase.org, and the newest version of the database is Release 22.1 (Accessed on 2025-06-22).

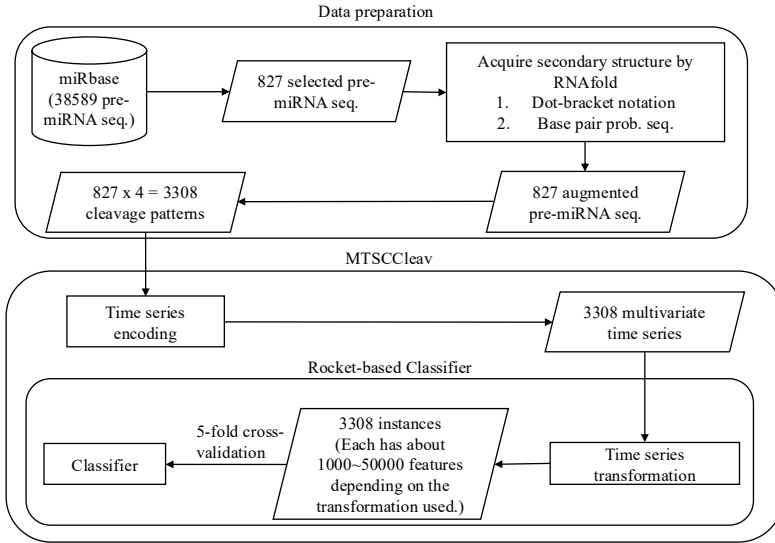


Fig. 2: The overall pipeline of this study. Symbol notations: Cylinder - Dataset, Rectangle - Process, Parallelogram - Input / Output, Rounded Rectangle - Component.

Accession	Name	Organism	Sequence	Mature miRNA 1	Mature miRNA 2
MI0000001	cel-let-7	Caenorhabditis elegans	<i>UACAC...UUCGA</i>	cel-let-7-5p 17:38 experimental	cel-let-7-3p 60:81 experimental
MI0000060	hsa-let-7a-1	Homo sapiens	<i>UGGGA...UCCUA</i>	hsa-let-7a-5p 6:27 experimental	hsa-let-7a-3p 57:77 experimental
MI0000114	hsa-mir-107	Homo sapiens	<i>CUCUC...ACAGA</i>	hsa-miR-107 50:72 experimental	NA
MI0000238	hsa-mir-196a-1	Homo sapiens	<i>GUGAA...UUCAC</i>	hsa-miR-196a-5p 7:28 experimental	hsa-miR-196a-1-3p 45:65 not experimental

Table 1: Selected representative records from miRBase. For the last two columns, the first line shows the name, the second line shows its location in the original sequence, and the third line indicates whether its existence has experimental evidence. The selected one is highlighted in **bold**.

126 Table 1 shows its four representative records. We first selected the records from
 127 humans (*Homo sapiens*). It resulted in 1917 records. To identify the actual locations
 128 of the two cleavage sites in the pri-miRNA sequence supported by experimental evi-
 129 dence, we selected records that have two mature miRNAs resulting from cleavage at
 130 the 5p arm and the 3p arm, both of which have experimental support. Hence, only
 131 “MI0000060” (“hsa-let-7a-1”) would be selected in the table. It would serve as our
 132 running example. The whole sequence of it is listed in Table 2. After the selection

process, we selected 827 experimental validated pre-miRNA sequences, each with its two mature miRNA products. This formed our dataset.

Sequence	Secondary Structure (In Dot-bracket notation)
1 UGGGA UGAGGUAGUAGGUUGUAUAGUU 27 28 UUAGGGUCACACCCACCACUGGGAGAU 54 55 AAC CUAUACAAUCUACUGUCUUUC CUA 80	1 (((((.((((((((((((())))))))) 27 28 UUAGGGUCACACCCACCACUGGGAGAU 54 55))))))))))))))))))))) 80
Base-pair probabilities sequence (the first 10 bases)	
1 (0.549, 0.946, 0.987, 0.987, 0.904) 5 6 (0.000 , 0.841, 0.974, 0.981, 0.890) 10	

Table 2: The whole sequence of “hsa-let-7a-1” and its predicted secondary structure by RNAfold. The corresponding positions of the two mature miRNAs and the probability of the unpaired “U” are highlighted in **bold**.

2.1.1 Argument the dataset with Secondary Structure information

We leveraged the predicted secondary structure of these sequences to enhance the accuracy of the classification. Recall that a specific three-dimensional (3D) structure is required for DNA, RNA, and protein to perform functions [15]. However, finding these 3D structures using experimental methods such as X-ray crystallography or nuclear magnetic resonance (NMR) is costly and time-consuming. Hence, prediction methods for such 3D structures are necessary and helpful for downstream analysis. However, predicting the 3D structures is challenging. One of the reasons is that there are some “nonconventional” base-pair interactions (e.g., noncanonical and rare A-G) that allow an RNA sequence to fold into a 3D structure, in addition to the (G, U) wobble pair, which is common and functionally important in RNA secondary structures. It makes the search space for prediction much larger than, in the 2D case, the secondary structure. The local structures of the 3D structures, the secondary structures, only focus on the conventional base-pair interactions [2]. Hence, predicting secondary structures is easier and faster. We employed RNAfold from the ViennaRNA Package⁶ to predict the secondary structure for a given pri-miRNA S [16]. RNAfold returns the secondary structure in the dot-bracket notation and a matrix of base-pair probabilities. The matrix is a square matrix with the side length $|S|$, where each entry m_{ij} is the probability of base s_i paired up with base s_j . Dot-bracket notation is a way of representing the secondary structure of S . Open parentheses “(“ (Close parentheses “)”)) indicates that the base is paired with a complementary base further (earlier) along in S . Dot “.” indicates that the base is unpaired. Equipped with the matrix, we can construct the base-pair probability sequence of S . The predicted secondary structure and the base-pair probability sequence of our running example are shown in Table 2.

⁶The latest stable release is Version 2.7.0 (Accessed on 2025-06-22).

159 **2.1.2 Extract cleavage patterns**

160 The locations of the two mature miRNAs on the whole sequence indicate the probable
 161 locations of the two cleavage sites. The 5p cleavage site must be beyond and near the
 162 ending location of the 5p mature miRNA. We deemed the immediate bond next to
 163 the 5p mature miRNA's ending position the 5p cleavage site, with the knowledge that
 164 the actual cleavage site may not be this immediate bond but rather the nearby bonds
 165 after it. The same applies to the 3p cleavage site. It is located at the immediate bond
 166 before the starting position of the 3p mature miRNA.

167 For each arm of each whole sequence, we extracted a 14-string⁷ with the cleavage
 168 site located at the center of the string. The first 7 nt (nucleotide) before the center are
 169 highlighted in **bold**. In our running example, it would be “**U**AUAGUUUUAGGU”
 170 for the 5p cleavage site and “**G**AGAUAAACAUACAC” for the 3p cleavage site.
 171 We refer to these 14-strings as cleavage patterns. We also generate non-cleavage
 172 patterns by selecting a 14-string with the center 6 nt away from the correspond-
 173 ing cleavage sites towards the corresponding mature miRNA [9, 10] for each arm
 174 of each whole sequence. So, in our running example, the 5p non-cleavage pat-
 175 tern would be “**A**GGUUGUAUAGUUU”. The 3p non-cleavage pattern would be
 176 “**A**CUAUACAAUCUAC”.

177 In conclusion, for a given pri-miRNA sequence, we can generate two cleavage pat-
 178 terns and two non-cleavage patterns. We call these four patterns simply the “four
 179 strings” of a given pri-miRNA. We also call each string a strand. The “four strings”
 of our running example are listed in Table 3.

	5p cleav	5p non-cleav	3p cleav	3p non-cleav
Input strand	U AUAGUUUUAGGU	A GGUUGUAUAGUUU	G AGAUAAACAUACAC	A CUAUACAAUCUAC
Complementary strand	AUAUCAA____UA	UCUAACAUACAA_	C_CUGUUGUAUAGU	UGAUUAUGUUGGAUG

Table 3: The first row shows the “four strings” of “hsa-let-7a-1”. Their complementary strands are shown in the second row. As a whole, they are referred to as the “eight strings”.

180
 181 We can construct the complementary strand of each of the strands in the “four
 182 strings” by finding the corresponding paired base for each of the bases in the input
 183 strand by considering the secondary structure information. We use “_” to denote the
 184 unpaired base in the complementary strand. For example, in Fig. 1, “UUAGG” in the
 185 5p cleavage pattern is unpaired, while other bases pair with some bases, the resulting
 186 complementary strand is “AUAUCAA____UA”. There is a loop/ budge there. We
 187 refer to the “four strings” and the four complementary strands together as the “eight
 188 strings” of the input pre-miRNA. It is also shown in Table 3.

⁷String with length = 14.

189 2.2 Time Series Encoding

190 A time series $T = t_1, t_2, \dots, t_n$ is a sequence of real-valued numbers⁸. A short contiguous
 191 region of T is called a subsequence. A subsequence $T(i : j) = t_i, t_{i+1}, \dots, t_j$ of a time
 192 series T is a shorter time series that starts from position i and ends at position j ,
 193 where $i < j$.

194 Strings and time series are temporal sequences. The difference between strings and
 195 time series lies in their behavioral attributes [17]. For strings, an entry is a letter from
 196 a predefined set called the alphabet. For example, the alphabet is $\{A, C, G, T\}$ in the
 197 DNA string, while $\{A, C, G, U\}$ in the RNA string. For time series, an entry is a real
 198 number. Unlike real numbers, there is no ordering in the alphabet unless some external
 199 domain knowledge is introduced.

200 The study of applying signal processing techniques to genomic data is called
 201 “Genomic Signal Processing” (GSP) [18, 19]. In the field of GSP, the time series rep-
 202 resentations of DNA strings are referred to as DNA numeric representations (DNR).
 203 Many DNRs have been proposed. We noted that DNA strings and RNA strings are
 204 equivalent from a computational standpoint. Many transformation methods designed
 205 for DNA can be applied to RNA by simply substituting T with U . We present nine
 encoding methods. The relationship among them is shown in Fig. 3.

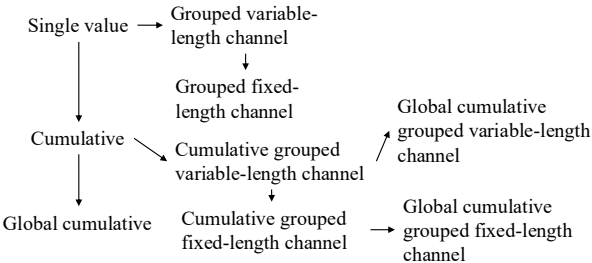


Fig. 3: Relationship of the proposed encoding methods.

206

207 2.2.1 Single value versus Cumulative

208 One of the simple, if not the simplest, encoding is to map the letters into numbers.
 209 Domain knowledge can be utilized. This approach is called the “Single value map-
 210 ping” [18, 20–23]. One single value is assigned to each of the letters. [24] employed
 211 the atomic number of each nucleotide as the transformed values, where $\{G = 78, A =$
 212 $70, C = 58, T = 66\}$. [25] used electron-ion interaction potential representation (EIIP)
 213 as such value, where $\{G = 0.0806, A = 0.1260, C = 0.1340, T = 0.1335\}$. Our goal is
 214 to transform the input strand and its complementary strand into time series, aiming
 215 to capture the information contained in these sequences and the secondary structure
 216 implied by them. We employed the following reasoning to assign the value:

⁸Unless otherwise specified, we denote entries of a time series (e.g., T) using the corresponding lowercase letter (e.g., t).

- 217 1. We employ the complementary property [22, 26] during encoding. Recall that in
 218 the base-pairing rules, G pairs with C to form three hydrogen bonds while A pairs
 219 with U^9 to form two hydrogen bonds. $G-C$ pairs are more stable than $A-U$ pairs. G
 220 (U) can be regarded as the “inverse” of C (A). We can preserve these base-pairing
 221 rules in the encoding by assigning G (A) and C (U) opposite values.
- 222 2. G and A have a two-ring structure. They are purines. C and U have a single-ring
 223 structure. They are pyrimidines. Hence, we put G and A (C and U) on the same
 224 side of the number line with zero in the middle.
- 225 3. The lower stability of $A-U$ pairs promotes strand separation, thereby facilitating
 226 the unwinding of the miRNA duplex during RISC loading. Regions rich in A and U
 227 are thus more likely to undergo strand selection and cleavage events. We assigned
 228 A (U) with a larger absolute value than G (C) to reflect this functional relevance.
 229 It aims to highlight sequence regions with higher cleavage potential.

230 It results in our baseline transformation method, namely “Single value mapping”,
 231 shown in row 1 of Table 4. S is the input strand. When we encode S without incor-
 232 porating the corresponding base-pair probability sequence P , we set $p_i = 1$ for all the
 233 entries of P . We use the first ten nucleotides of the complementary strand of the 3p
 234 cleav of “hsa-let-7a-1”, as shown in Table 3 as S in the examples in Table 4.

235 With the assigned value to each nucleotide defined in single-value mapping, we can
 236 compute a cumulative sum of those values over time. It captures the aggregated signal
 237 by accumulating past events, allowing us to focus on the trend [27, 28]. We named
 238 this method as “Cumulative mapping”, shown in row 4 of Table 4.

239 2.2.2 Grouped variable-length channel versus Grouped 240 local-length channel

241 We can transform the input strand into a multivariate time series with two channels
 242 using grouped binary encoding, where nucleotides are grouped into (A , U) and (G ,
 243 C). It releases our third assumption that A (U) has a larger absolute value than
 244 G (C). We proposed two variations. The first one allows the output to be variable-
 245 length sequences per channel, depending on group-specific occurrences. The second
 246 one always returns two resulting sequences of fixed length. Two variations extended
 247 from single value mapping are shown in rows 2 and 3, while those extended from
 248 cumulative mapping are shown in rows 5 and 6 in Table 4.

249 2.2.3 Global cumulative versus Local Cumulative

250 In cumulative mapping and its variations, we can choose where to start the accumu-
 251 lation. For a given subsequence S' of the whole sequence S , accumulation can start
 252 from the beginning of S even if only S' is used downstream. Or it can begin just at
 253 the start of the S' . The first one preserves the global context. It can be useful when
 254 previous nucleotides (those before S') influence later interpretation. The second one
 255 focuses solely on local history in S' , ignoring global history. It is helpful if the previous
 256 nucleotides do not affect the chemical property of S' .

⁹In DNA, A pairs with T .

space is added for indentation.

	Encoding	Algorithm	Example
1	Single value mapping [18, 20–23]	<pre> for i = 1 to S : $t_i = \begin{cases} 2 \cdot p_i & \text{if } s_i = A \\ 1 \cdot p_i & \text{if } s_i = G \\ -1 \cdot p_i & \text{if } s_i = C \\ -2 \cdot p_i & \text{if } s_i = U \\ 0 & \text{otherwise} \end{cases}$ return T </pre>	Without base-pair probability sequence: $T = -1, 0, -1, -2, 1, -2, -2, 1, 2, -2$ With base-pair probability sequence: $T = -0.843, 0.000, -0.807, -1.614, 0.793, -1.829, -1.963, 1.000, 1.999, -1.998$
2	Grouped variable-length channel mapping	<pre> j = 1, k = 1 for i = 1 to S : $t_j^1 = \begin{cases} 1 \cdot p_i & \text{if } s_i = A \\ -1 \cdot p_i & \text{if } s_i = U \\ 0 & \text{otherwise} \end{cases}$ $t_k^2 = \begin{cases} 1 \cdot p_i & \text{if } s_i = G \\ -1 \cdot p_i & \text{if } s_i = C \\ \text{if } (s_i = G) \text{ or } (s_i = C): \\ \quad \text{increment } k \text{ by 1} \\ \text{else:} \\ \quad \text{increment } j \text{ by 1} \end{cases}$ return T^1, T^2 </pre>	Without base-pair probability sequence: $T^1 = 0, -1, -1, -1, 1, -1$ $T^2 = -1, -1, 1, 1$ With base-pair probability sequence: $T^1 = 0.000, -0.807, -0.914, -0.982, 0.999, -0.999$ $T^2 = -0.843, -0.807, 0.793, 1.000$
3	Grouped fixed-length channel mapping	<pre> for i = 1 to S : $t_i^1 = \begin{cases} 1 \cdot p_i & \text{if } s_i = A \\ -1 \cdot p_i & \text{if } s_i = U \\ 0 & \text{otherwise} \end{cases}$ $t_i^2 = \begin{cases} 1 \cdot p_i & \text{if } s_i = G \\ -1 \cdot p_i & \text{if } s_i = C \\ 0 & \text{otherwise} \end{cases}$ return T^1, T^2 </pre>	Without base-pair probability sequence: $T^1 = 0, 0, -1, 0, -1, -1, 0, 1, -1$ $T^2 = -1, 0, -1, 0, 1, 0, 0, 1, 0, 0$ With base-pair probability sequence: $T^1 = 0.000, 0.000, 0.000, -0.807, 0.000, -0.914, -0.982, 0.000, 0.999, -0.9999$ $T^2 = -0.843, 0.000, -0.807, 0.000, 0.793, 0.000, 0.000, 1.000, 0.000, 0.000$
4	Cumulative mapping [27, 28]	<pre> t_1 = 0 for i = 1 to S : $t_{i+1} = \begin{cases} t_i + 2 \cdot p_i & \text{if } s_i = A \\ t_i + 1 \cdot p_i & \text{if } s_i = G \\ t_i - 1 \cdot p_i & \text{if } s_i = C \\ t_i - 2 \cdot p_i & \text{if } s_i = U \\ t_i & \text{otherwise} \end{cases}$ return $T // T = S + 1$ </pre>	Without base-pair probability sequence: $T = 0, -1, -1, -2, -4, -3, -5, -7, -6, -4, -6$ With base-pair probability sequence: $T = 0.000, -0.843, -0.843, -1.650, -3.265, -2.471, -4.300, -6.263, -5.264, -3.265, -5.263$
5	Cumulative grouped variable-length channel mapping	<pre> t_1^1 = 0, t_1^2 = 0 j = 1, k = 1 for i = 1 to S : $t_{j+1}^1 = \begin{cases} t_j^1 + 1 \cdot p_i & \text{if } s_i = A \\ t_j^1 - 1 \cdot p_i & \text{if } s_i = U \\ t_j^1 & \text{if } s_i = - \end{cases}$ $t_{k+1}^2 = \begin{cases} t_k^2 + 1 \cdot p_i & \text{if } s_i = G \\ t_k^2 - 1 \cdot p_i & \text{if } s_i = C \\ \text{if } (s_i = G) \text{ or } (s_i = C): \\ \quad \text{increment } k \text{ by 1} \\ \text{else:} \\ \quad \text{increment } j \text{ by 1} \end{cases}$ return T^1, T^2 </pre>	Without base-pair probability sequence: $T^1 = 0, -1, -2, -3, -2, -3$ $T^2 = 0, -1, -2, -1, 0$ With base-pair probability sequence: $T^1 = 0.000, -0.807, -1.722, -2.703, -1.704, -2.703$ $T^2 = 0.000, -0.843, -1.650, -0.857, 0.143$
6	Cumulative grouped fixed-length channel mapping	<pre> t_1^1 = 0, t_1^2 = 0 for i = 1 to S : $t_{i+1}^1 = \begin{cases} t_i^1 + 1 \cdot p_i & \text{if } s_i = A \\ t_i^1 - 1 \cdot p_i & \text{if } s_i = U \\ t_i^1 & \text{otherwise} \end{cases}$ $t_{i+1}^2 = \begin{cases} t_i^2 + 1 \cdot p_i & \text{if } s_i = G \\ t_i^2 - 1 \cdot p_i & \text{if } s_i = C \\ t_i^2 & \text{otherwise} \end{cases}$ return $T^1, T^2 // T^1 = T^2 = S + 1$ </pre>	Without base-pair probability sequence: $T^1 = 0, 0, 0, -1, -1, -2, -3, -3, -2, -3$ $T^2 = 0, -1, -1, -2, -2, -1, -1, 0, 0, 0$ With base-pair probability sequence: $T^1 = 0.000, 0.000, 0.000, 0.000, -0.807, -0.807, -1.722, -2.703, -2.703, -1.704, -2.703$ $T^2 = 0.000, -0.843, -0.843, -1.650, -1.650, -0.857, -0.857, -0.857, 0.143, 0.143, 0.143$

Table 4: Time series encoding. P is the corresponding base-pair probability sequence of S . $p_i = 1$ if we encode S without base-pair probability sequence.

Consider $T = 0, -1, \dots, -6$ of the input string S in “Cumulative mapping” in Table 4, which accumulates from 0. S is the suffix with length = 10 of the constructed complementary strand of $S(1 : 63)$ in Fig. 1. If we start the accumulation from the first entry of the constructed complementary strand instead, it will yield a different result. Suppose the last entry of the time series encoded in the cumulative mapping of the constructed complementary strand is 2, the time series encoded in the “Global cumulative mapping” for S would accumulate from 2 instead of 0. The result is $T = 2, 1, \dots, -4$. Note that it has the same trend as the original T . This “Global cumulative” concept can be applied to every cumulative-based method, as shown in Fig. 3.

2.2.4 Incorporating base-pair probabilities

We can incorporate the base-pair probabilities P in the encoding by thinking of it as the weight or confidence p_i in the value assignment of each nucleotide s_i . It is implemented by multiplying the base-pair probability p_i of the nucleotide s_i with the assigned value of the kind of nucleotide of s_i during encoding, as shown in Table 4.

2.2.5 Transforming the secondary structure into time series

We can transform the secondary structure in the dot-bracket notation into a time series by “Single value mapping”, where “(” maps to 1, “.” maps to 0, and “)” maps to -1.

2.3 Time series classification

In univariate time series classification, an instance in the dataset consists of a time series $x = x_1, x_2, \dots, x_m$ with m observations and a discrete class label y , which takes c possible values [29, 30]. If $c = 2$, we refer to binary classification. If $c > 2$, we refer to multi-class classification. In multivariate time series classification, the time series is not a single sequence but a list of sequences. Each sequence is called a channel. There are many classifiers defined for time series data, including distance-based, feature-based, interval-based, shapelet-based, dictionary-based, convolution-based, and deep learning-based classifiers. Additionally, two or more of the above approaches can be combined, resulting in hybrid approaches [29–31]. We employed convolution-based classifiers due to their simplicity and accuracy.

2.3.1 Convolution-based classifiers

Convolution-based classifiers first use randomly parameterized kernels to perform convolutions on the original time series T . A kernel is referred to as parameterized because its behavior is governed by a set of parameters, which will be discussed in detail later. Convolution is an operation to transform T to another time series M , where M is called the activation map. Its entry M_i is calculated by applying a kernel ω with length l to T at position i , defined as follows:

$$M_i = A(i : i + l - 1) * \omega = \sum_{j=0}^{l-1} A_{i+j} \cdot \omega_{1+j}$$

287 To note, $|A(i : i + l - 1)| = |\omega| = l$. Entries M_i 's are calculated by sliding ω across
 288 T and computing a dot product. Additionally, although the original paper used the
 289 term “convolution” to refer to the above operation, “cross-correlation” may be a more
 290 suitable term for this operation. Recall T with length m has $(m-l+1)$ sliding windows
 291 of length l , given that the increment is 1^{10} , which defines the length of M .

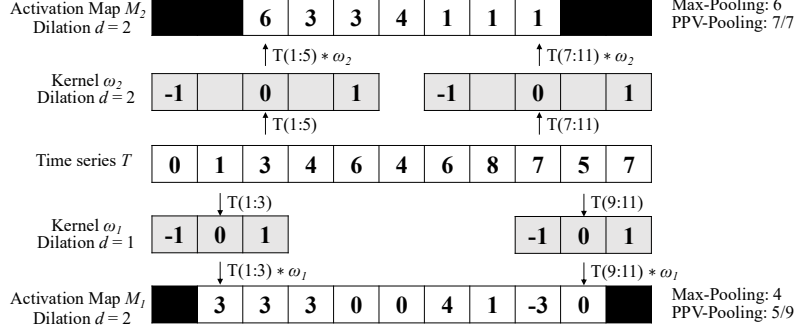


Fig. 4: Features generation in the transformation

292 Fig. 4 shows two kernels ω_1 and ω_2 with lengths 3 and 5, respectively. Each of
 293 which performs a convolution with T and returns two activation maps, M^1 and M^2 ,
 294 respectively. For example, $M_1^1 = T(1 : 3) * \omega_1 = 3$. By sliding ω_1 one time stamp at a
 295 time, an activation map M^1 with length $= (m - l + 1) = 11 - 3 + 1 = 9$ is obtained.
 296 Then, pooling operations, such as the maximum (MAX) and proportion of positive
 297 values (PPV), are applied on M^1 to derive the summary features. In Fig. 4, MAX
 298 and PPV are applied on M^1 and M^2 . The summary features of M^1 are 4 and 5/9,
 299 which correspond to MAX and PPV, respectively. Dilation refers to a method that
 300 enables a kernel to cover a larger portion by creating empty spaces between entries in
 301 the kernel. The dilation d of ω_2 is 2. It introduces a gap of 1 in every two values of ω_2 .

302 The most popular convolution-based approach is the Random Convolutional Ker-
 303 nel Transform (ROCKET) [32]. It generates a large number of randomly parameterized
 304 kernels, ranging from thousands to tens of thousands. The kernel's parameters include
 305 length, weights (the entries inside the kernel), bias (the value added to the result of
 306 the convolution operation), and dilation. Additionally, padding can be applied to T at
 307 the start and end, ensuring M has the same length as the input. To note, T , M_1 , and
 308 M_2 in Fig. 4 have different lengths. The summary statistics of the activation map are
 309 obtained through two pooling operations: MAX and PPV. Hence, for k kernels, the
 310 transformed data has $2k$ features. The default value of k is 10000. The feature vector
 311 size is then 20000.

312 There are two extensions of ROCKET. They are MiniROCKET [33] and Mu-
 313 tiROCKET [34]. MiniROCKET removes unnecessary operations and many of the
 314 random components in the definition of kernels used by ROCKET. It speeds up Rocket
 315 by over an order of magnitude with no significant difference in accuracy, making the

¹⁰One step to the right per time

316 classifier almost deterministic. For example, the kernel length is fixed, and only two
 317 weight values are used. Only PPV is used for the summary statistics. MultiROCKET
 318 is extended from MiniROCKET. The main improvement of it is to extract features
 319 from first-order differences as defined in Table 5 and add three new pooling opera-
 320 tions [34]. The three added operations are mean of positive values (MPV), mean of
 321 indices of positive values (MIPV) and longest stretch of positive values (LSPV).

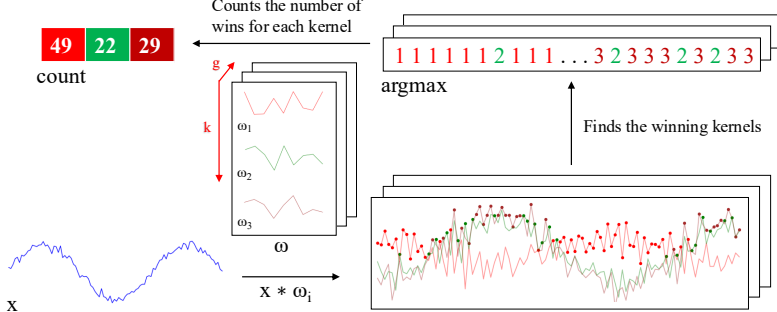


Fig. 5: Convolutions of HYDRA for each input time series with a set of random kernels w , organized into g groups with k kernels each.

322 The HYbrid Dictionary-ROCKET Architecture (Hydra) combines dictionary-
 323 based and convolution-based models [35]. Similar to ROCKET-based classifiers, it
 324 uses random kernels to extract features from the input time series. But it groups the
 325 kernels into g groups of k kernels each, as shown in Fig. 5. Each time series is passed
 326 through all the groups. For each group of kernels, we slide them across T and compute
 327 the dot product at each timestamp. Recall that the dot product of two input vectors
 328 (x and w_i) has the maximum value when the two vectors align in the same direc-
 329 tion and the minimum value when they are oriented in opposite directions. We record
 330 the kernel that best matches the subsequence of T at each timestamp in each group
 331 (i.e., argmax). We refer to these kernels as the winning kernels. This results in a k -
 332 dimensional count vector for each of the g groups, where $k = 3$ in Fig. 5. This results
 333 in a total of $g \times k$ features, with default values of $g = 64$ and $k = 8$. It uses a total
 334 of $k \times g = 512$ kernels per dilation. In addition to recording the kernel with the max-
 335 imum response, we can also record the kernel with the minimum response, knowing
 336 that this kernel will be the best match with the “inverted” subsequence of T . Hydra
 337 is applied to both the original time series and its first-order differences. Hydra gener-
 338 ated approximately 1000 features for each instance in our dataset. [35] found that it
 339 can improve the accuracy by concatenating features generated from Hydra with those
 340 from MultiRocket. This classifier is called MultiROCKET-Hydra.

341 These five classifiers share the same simple design pattern. It involves the overpro-
 342 duction of features followed by a selection strategy. A large number of features (1000
 343 ~ 50000) are generated for each instance. The features are then fed into a simple linear
 344 classifier. It determines which features are most useful and returns the final classifica-
 345 tion result. A ridge classifier is used in this study. It is a linear classifier that extends

ridge regression to classification tasks by applying a threshold to the predicted values.
 It uses L2 regularization to prevent overfitting. The regularization strength is selected
 by internal cross-validation. A Ridge classifier is suggested for small datasets, as in
 our case, while a logistic regression classifier is suggested for large datasets [31].

While these five classifiers are often referred to as classifiers, they are technically time series transformation methods for generating features that are then fed to a downstream classifier. The comparison of them is shown in Table 5. For MiniROCKET and MultiROCKET, the bias is determined from the convolution output, and the dilation depends on the length of the input time series [33]. The main differences among ROCKET-based classifiers lie in how the summary features are generated. The generation of the summary features depends on:

1. Kernels, which are defined based on the parameters, which consist of kernel length, kernel weights, bias, and dilation.
2. The way that padding applies to T , which leads to activation maps with different lengths.
3. The pooling operations, which are used in extracting features on the activation map.

New Table

F

	ROCKET	MiniROCKET	MultiROCKET	Hydra
kernel length	{7, 9, 11}	9	9	9
kernel weights	$\mathcal{N}(0, 1)$	{-1, 2}	{-1, 2}	$\mathcal{N}(0, 1)$
bias	$\mathcal{U}(0, 1)$	from output	from output	none
dilation	random	fixed (input-relative)	fixed (input-relative)	random
padding	random	fixed	fixed	always
pooling operations	MAX, PPV	PPV	PPV, MPV, MIPV, LSPV	Response per Kernel/Group
1 st order difference	no	no	yes	yes
feature vector size	20k	10k	50k	relative to input

Table 5: Comparison of rocket-based classifiers [31]. $\mathcal{N}(0, 1)$: a standard normal distribution, $\mathcal{U}(0, 1)$: a uniform distribution between 0 and 1, 1st order difference: $\Delta T = t_2 - t_1, t_3 - t_2, \dots, t_n - t_{n-1}$.

2.4 Evaluation metrics

To evaluate the performance of our time series-based classification (MTSC) model, we adopted five standard classification metrics. They are Accuracy (Acc), Specificity (Sp), Sensitivity (Sn), F1 score (F1), and Matthews Correlation Coefficient (MCC) [36].

$$\begin{aligned}
 Acc &= \frac{TP + TN}{TP + TN + FP + FN} \\
 Sp &= \frac{TN}{TN + FP} \\
 Sn &= \frac{TP}{TP + FN}
 \end{aligned}$$

$$F1 = \frac{2 \times TP}{2 \times TP + FP + FN}$$

$$MCC = \frac{TP \times TN - FP \times FN}{\sqrt{(TP + FP)(TP + FN)(TN + FP)(TN + FN)}}$$

364 Where TP, TN, FP, and FN are the number of true positives, true negatives, false
 365 positives, and false negatives, respectively.

To extend a binary metric to multi-class problems, we can treat the data as a collection of binary problems, one for each class. One class is treated as positive while the other classes are treated as negative. Then, the multi-class metrics can be obtained by averaging binary metric calculations across the set of classes. There are different ways to do the averaging. Here, we adopted a macro-averaging approach. It treats each class equally and calculates the mean of the binary metrics. To use *MCC* in the multiclass case, it can be defined in terms of a confusion matrix C for K classes, where $C_{i,j}$ is the number of observations that are actually in class i and predicted to be in class j [37].

$$MCC_{multi} = \frac{c \times s - \sum_k^K p_k \times t_k}{\sqrt{(s^2 - \sum_k^K p_k^2) \times (s^2 - \sum_k^K t_k^2)}}$$

366 Where $t_k = \sum_i^K C_{i,k}$ (The number of times class k actually occurred), $p_k = \sum_i^K C_{k,i}$
 367 (The number of times class k was predicted), $c = \sum_k^K C_{k,k}$ (The total number of
 368 samples correctly predicted) and $s = \sum_i^K \sum_j^K C_{i,j}$ (The total number of samples).

369 3 Results

370 In all experiments, the models were trained and tested using 5-fold cross-validation.
 371 We retrieved 827 empirically validated sequences of pre-miRNAs. There are 5p arm
 372 and 3p arm in each sequence. For each arm, we defined a cleavage pattern and a non-
 373 cleavage pattern. Three datasets, namely “5p arm”, “3p arm”, and “multi-class” were
 374 constructed by these patterns. We refer to the cleavage patterns as positive instances
 375 and the non-cleavage patterns as negative instances. The 5p arm dataset comprises
 376 827 positive instances and an equal number of negative instances. The 5p arm and 3p
 377 arm datasets are binary-class datasets. The multi-class dataset comprises all patterns
 378 from both the 5p arm and the 3p arm. There are 827 “5p” instances¹¹, 827 “3p”
 379 instances, and 1654 negative instances.

380 For every fold in 5-fold cross-validation, the dataset was divided into a training
 381 set and a test set with sizes of 80% and 20% of the whole dataset, respectively. We
 382 kept the class distribution approximately the same in each fold, as it is in the original
 383 dataset. In each fold derived from the 5p arm and 3p arm datasets, the training set
 384 has a size of 1323, and the test set has a size of 331. In each fold derived from the
 385 multi-class dataset, the training set has a size of 2262, and the test set has a size of
 386 662. We reported the average of the five classification metrics.

¹¹cleavage patterns from the 5p arm

387 The ROCKET-based classifiers require all channels in the multivariate time series
388 to have equal length. We applied padding to the shorter channels using the constant
389 value 100, which does not appear in the original time series. It ensures the padding
390 does not introduce ambiguity or interfere with the semantic meaning of the encoded
391 nucleotide signals.

392 3.1 Channel ablation study

393 We utilized three types of data as the input features for each instance. They are
394 (1) the RNA sequence, which consists of the primary strand and its complementary
395 strand, (2) the secondary structure information, and (3) the base-pair probability
396 sequence. To input the data into our time series-based classifiers, we converted them
397 into multivariate time series. The primary strand and its complementary strand are
398 each encoded into one or two channels, using the encoding methods in Tables 4. For
399 example, single value mapping encodes a strand in one channel, while grouped variable-
400 length channel mapping encodes in two channels. The secondary structure information
401 is converted into a univariate time series. The base-pair probability sequence is already
402 in numerical form and does not require further transformation. It can be used either as
403 a standalone channel or incorporated into the encoding of the complementary strand.
404 We performed a channel ablation study to determine the most informative combination
405 of the above channels.

406 We referred to the multivariate time series that consists of the channels from the
407 RNA sequence only as the baseline setting. We added the other channels to this
408 baseline. It leads to the following configurations (cfgs):

- 409 1. (cfg 1) Baseline: Time series derived only from the RNA sequence.
- 410 2. (cfg 2) Baseline + Secondary structure: Baseline + time series representation of
411 the secondary structure.
- 412 3. (cfg 3) Baseline + Base-pair probability (Standalone): Baseline + the base-pair
413 probability sequence as a standalone channel.
- 414 4. (cfg 4) Baseline + Base-Pair probability (Incorporated): Baseline with the base-pair
415 probability sequence incorporated into the encoding of the complementary strand.

416 We used single value mapping as the encoding method. Table 6 shows the result.
417 From the table, we can see that the addition of secondary structure, base-pair proba-
418 bility as a standalone channel, and base-pair probability incorporated in the encoding
419 of the complementary strand can improve the performance. We plotted the critical
420 difference (CD) diagram to visualize Table 6 to make the performances of different
421 combinations more obvious. In CD diagrams, lower-ranked methods (toward the right)
422 are better. A horizontal bar connecting combinations indicates no statistically signif-
423 icant difference. From Figure 6, we can see that including time series derived from
424 secondary structure information and base-pair probability as a separate channel can
425 significantly improve the performance of the classifiers. Incorporating the base-pair
426 probability sequence in the time series encoding of the complementary strand can also
427 improve the classifier, but to a minor degree compared to serving as a standalone chan-
428 nel. In our downstream analysis, we adopted the combination of RNA sequence time

Classifier	5p arm				3p arm				multi-class							
	Acc	Sp	Sn	F1	MCC	Acc	Sp	F1	MCC	Acc	Sp	Sn	F1	MCC		
Baseline (cfg 1)	ROCKET	0.781	0.743	0.819	0.789	0.563	0.790	0.773	0.807	0.793	0.580	0.717	0.838	0.685	0.700	0.538
	MiniROCKET	0.755	0.728	0.782	0.762	0.512	0.788	0.781	0.794	0.789	0.576	0.685	0.823	0.653	0.662	0.486
	MultiROCKET	0.784	0.767	0.801	0.787	0.568	0.803	0.792	0.814	0.805	0.606	0.691	0.830	0.667	0.672	0.501
	Hydra	0.830	0.800	0.860	0.835	0.663	0.808	0.797	0.820	0.810	0.617	0.731	0.844	0.696	0.712	0.560
	MultiROCKET-Hydra	0.796	0.778	0.815	0.800	0.594	0.807	0.767	0.816	0.808	0.614	0.701	0.836	0.681	0.686	0.520
Baseline + Secondary Structure (cfg 2)	ROCKET	0.847	0.832	0.862	0.849	0.695	0.855	0.842	0.868	0.857	0.711	0.836	0.907	0.828	0.833	0.736
	MiniROCKET	0.825	0.807	0.843	0.827	0.655	0.822	0.802	0.843	0.826	0.646	0.823	0.900	0.812	0.818	0.715
	MultiROCKET	0.812	0.803	0.822	0.814	0.626	0.824	0.809	0.839	0.826	0.649	0.796	0.888	0.791	0.792	0.673
	Hydra	0.845	0.816	0.873	0.849	0.691	0.846	0.817	0.874	0.850	0.693	0.830	0.901	0.814	0.826	0.724
	MultiROCKET-Hydra	0.817	0.809	0.826	0.819	0.635	0.825	0.816	0.834	0.826	0.652	0.803	0.891	0.798	0.800	0.684
Baseline + Base-pair probability (Standalone) (cfg 3)	ROCKET	0.842	0.828	0.855	0.844	0.684	0.855	0.856	0.854	0.855	0.710	0.795	0.885	0.783	0.789	0.670
	MiniROCKET	0.817	0.820	0.814	0.816	0.634	0.836	0.834	0.838	0.836	0.673	0.772	0.872	0.757	0.764	0.632
	MultiROCKET	0.822	0.813	0.832	0.824	0.645	0.825	0.831	0.820	0.824	0.651	0.758	0.866	0.747	0.750	0.612
	Hydra	0.846	0.827	0.865	0.849	0.693	0.851	0.840	0.861	0.852	0.702	0.789	0.879	0.769	0.780	0.658
	MultiROCKET-Hydra	0.822	0.809	0.834	0.824	0.644	0.835	0.840	0.830	0.834	0.670	0.759	0.866	0.746	0.750	0.611
Baseline + Base-pair probability (Incorporated) (cfg 4)	ROCKET	0.799	0.771	0.827	0.805	0.600	0.809	0.786	0.832	0.813	0.610	0.737	0.850	0.712	0.724	0.573
	MiniROCKET	0.776	0.756	0.797	0.781	0.554	0.801	0.808	0.794	0.799	0.603	0.705	0.835	0.675	0.684	0.521
	MultiROCKET	0.814	0.801	0.828	0.817	0.630	0.816	0.812	0.820	0.816	0.634	0.726	0.848	0.706	0.712	0.556
	Hydra	0.822	0.787	0.857	0.828	0.647	0.834	0.828	0.840	0.835	0.669	0.759	0.862	0.734	0.746	0.608
	MultiROCKET-Hydra	0.814	0.802	0.820	0.817	0.629	0.820	0.825	0.816	0.819	0.642	0.736	0.853	0.717	0.723	0.874

Table 6: Channel ablation study.

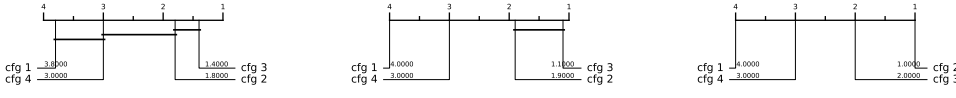


Fig. 6: CD diagrams of channel ablation study.

series, secondary structure time series, and base-pair probability time series as our multivariate time series input, with 4 to 6 channels, depending on the encoding used.

3.2 Predictive performance

The experiment was conducted on three datasets: the 5p arm, the 3p arm, and the multi-class datasets. Recall that we have nine encoding methods and five ROCKET-based classifiers. It results in 45 combinations of encoding methods and classifiers.

The result is shown in Table 7. The best combination of encoding method and classifier is shown in Table 8. For the 5p arm dataset, the best combination is “Global Cumulative grouped fixed-length channel mapping + ROCKET”. For all five classification metrics, it outperforms the state-of-the-art (SOTA) method, DiCleave. For the 3p arm dataset, the best combination is “Global Cumulative grouped fixed-length channel mapping + ROCKET”. Out of the five classification metrics, it outperforms DiCleave, except in specificity. For the multi-class dataset, the best combination is “Global Cumulative grouped fixed-length channel mapping + ROCKET”. For all five classification metrics, it outperforms DiCleave. Note that for the 3p arm and the multi-class datasets, the combination of “Cumulative grouped fixed-length channel mapping + ROCKET” also attains the best result.

To summarize Table 7, we plot the CD diagrams for finding the best classifier, as shown in Figure 7, and the best encoding method, as shown in Figure 8.

	Classifier	5p arm					3p arm					multi-class				
		Acc	Sp	Sn	F1	MCC	Acc	Sp	Sn	F1	MCC	Acc	Sp	Sn	F1	MCC
Single value mapping (enc 1)	ROCKET	0.849	0.842	0.857	0.851	0.699	0.863	0.854	0.873	0.865	0.727	0.853	0.917	0.847	0.851	0.764
	MiniROCKET	0.823	0.809	0.837	0.825	0.647	0.823	0.828	0.817	0.822	0.647	0.835	0.906	0.828	0.833	0.735
	MultiROCKET	0.821	0.802	0.840	0.824	0.643	0.839	0.826	0.852	0.841	0.679	0.811	0.894	0.806	0.809	0.697
	Hydra	0.843	0.820	0.867	0.847	0.688	0.838	0.819	0.857	0.841	0.677	0.831	0.901	0.815	0.827	0.727
Grouped variable-length channel mapping (enc 2)	ROCKET	0.835	0.826	0.844	0.836	0.670	0.855	0.849	0.861	0.856	0.710	0.846	0.913	0.839	0.844	0.752
	MiniROCKET	0.843	0.833	0.853	0.844	0.686	0.831	0.821	0.842	0.833	0.663	0.837	0.907	0.828	0.834	0.737
	MultiROCKET	0.819	0.809	0.828	0.820	0.638	0.817	0.814	0.820	0.818	0.634	0.890	0.894	0.806	0.808	0.695
	Hydra	0.825	0.780	0.869	0.832	0.653	0.811	0.769	0.854	0.819	0.626	0.818	0.892	0.765	0.812	0.705
Grouped fixed-length channel mapping (enc 3)	ROCKET	0.851	0.843	0.859	0.852	0.702	0.863	0.850	0.875	0.864	0.726	0.849	0.915	0.843	0.847	0.757
	MiniROCKET	0.844	0.836	0.853	0.845	0.689	0.840	0.826	0.855	0.843	0.682	0.851	0.915	0.844	0.849	0.760
	MultiROCKET	0.831	0.815	0.849	0.834	0.663	0.824	0.813	0.836	0.826	0.649	0.811	0.896	0.808	0.803	0.698
	Hydra	0.848	0.816	0.880	0.853	0.699	0.862	0.830	0.884	0.864	0.724	0.843	0.908	0.837	0.839	0.746
Grouped fixed-length channel mapping (enc 4)	ROCKET	0.850	0.834	0.866	0.852	0.701	0.863	0.855	0.871	0.864	0.726	0.852	0.915	0.842	0.850	0.762
	MiniROCKET	0.840	0.821	0.860	0.843	0.682	0.840	0.837	0.844	0.841	0.682	0.843	0.911	0.835	0.840	0.747
	MultiROCKET	0.822	0.809	0.834	0.834	0.644	0.832	0.830	0.834	0.832	0.665	0.820	0.898	0.810	0.816	0.709
	Hydra	0.848	0.819	0.878	0.853	0.698	0.853	0.856	0.869	0.855	0.705	0.845	0.910	0.830	0.841	0.749
Cumulative grouped variable-length channel mapping (enc 5)	ROCKET	0.843	0.821	0.866	0.847	0.688	0.856	0.840	0.871	0.864	0.712	0.855	0.916	0.843	0.851	0.766
	MiniROCKET	0.845	0.826	0.865	0.848	0.691	0.836	0.833	0.838	0.836	0.672	0.840	0.909	0.833	0.838	0.742
	MultiROCKET	0.826	0.814	0.836	0.828	0.654	0.815	0.820	0.810	0.814	0.631	0.826	0.902	0.820	0.824	0.721
	Hydra	0.850	0.819	0.880	0.854	0.701	0.834	0.807	0.861	0.838	0.669	0.833	0.903	0.818	0.829	0.731
Cumulative grouped fixed-length channel mapping (enc 6)	ROCKET	0.856	0.836	0.876	0.858	0.712	0.870	0.861	0.879	0.871	0.741	0.863	0.921	0.852	0.860	0.780
	MiniROCKET	0.856	0.837	0.874	0.858	0.712	0.842	0.830	0.845	0.843	0.685	0.845	0.912	0.837	0.843	0.751
	MultiROCKET	0.820	0.802	0.830	0.824	0.642	0.798	0.798	0.798	0.798	0.597	0.805	0.894	0.806	0.807	0.694
	Hydra	0.850	0.814	0.885	0.855	0.701	0.855	0.840	0.869	0.857	0.711	0.847	0.910	0.831	0.843	0.752
Global Cumulative mapping (enc 7)	ROCKET	0.850	0.834	0.866	0.852	0.701	0.863	0.855	0.871	0.864	0.726	0.852	0.915	0.842	0.850	0.762
	MiniROCKET	0.847	0.832	0.862	0.849	0.695	0.848	0.839	0.857	0.850	0.697	0.845	0.911	0.836	0.843	0.750
	MultiROCKET	0.827	0.819	0.834	0.828	0.653	0.847	0.842	0.853	0.848	0.695	0.825	0.901	0.817	0.822	0.718
	Hydra	0.851	0.821	0.880	0.855	0.703	0.861	0.848	0.874	0.863	0.722	0.847	0.911	0.834	0.844	0.753
Global Cumulative grouped variable-length channel mapping (enc 8)	ROCKET	0.837	0.834	0.839	0.837	0.674	0.834	0.830	0.849	0.844	0.688	0.832	0.905	0.823	0.829	0.730
	MiniROCKET	0.856	0.835	0.876	0.858	0.712	0.870	0.861	0.879	0.871	0.741	0.863	0.921	0.852	0.860	0.780
	MultiROCKET	0.829	0.824	0.834	0.830	0.654	0.843	0.830	0.849	0.844	0.688	0.832	0.907	0.828	0.832	0.734
	Hydra	0.856	0.834	0.876	0.858	0.712	0.870	0.861	0.879	0.871	0.741	0.863	0.921	0.852	0.860	0.780
Global Cumulative grouped fixed-length channel mapping (enc 9)	ROCKET	0.857	0.845	0.876	0.859	0.713	0.870	0.861	0.879	0.871	0.741	0.863	0.921	0.852	0.860	0.780
	MiniROCKET	0.829	0.825	0.833	0.830	0.658	0.820	0.816	0.823	0.820	0.640	0.819	0.900	0.816	0.817	0.710
	MultiROCKET	0.856	0.817	0.894	0.861	0.713	0.859	0.838	0.880	0.862	0.719	0.846	0.911	0.832	0.843	0.752
	Hydra	0.829	0.824	0.834	0.830	0.658	0.822	0.825	0.819	0.821	0.644	0.827	0.904	0.823	0.824	0.722

Table 7: Performance on the 45 combinations between encoding methods and the ROCKET-based classifiers.

Dataset	Methods	Acc	Sp	Sn	F1	MCC	Time (s)
5p arm	enc 9 + MiniROCKET	0.857	0.845	0.870	0.859	0.715	0.787
	DiCleave	0.818	0.790	0.846	0.822	0.653	21.249
3p arm	enc 9 + ROCKET	0.870	0.861	0.879	0.871	0.741	4.311
	enc 7 + MiniROCKET	0.848	0.839	0.852	0.850	0.697	0.989
	DiCleave	0.854	0.891	0.817	0.847	0.715	15.919
multi-class	enc 9 + ROCKET	0.863	0.921	0.852	0.860	0.780	12.208
	enc 3 + MiniROCKET	0.851	0.915	0.844	0.849	0.760	4.550
	DiCleave	0.820	0.895	0.804	0.815	0.710	131.151

Table 8: Comparative analysis between MTSCCleav with the best combination of the encoding method and classifier, with the SOTA, DiCleave, on the three datasets. The best results of using MiniROCKET have also been shown to compare the computational efficiency.

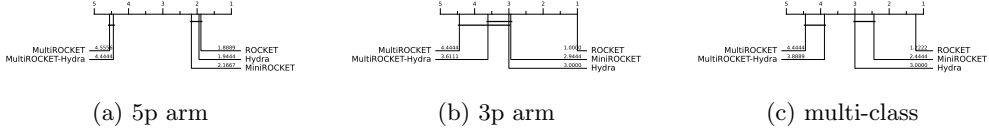


Fig. 7: CD diagrams to compare different classifiers.

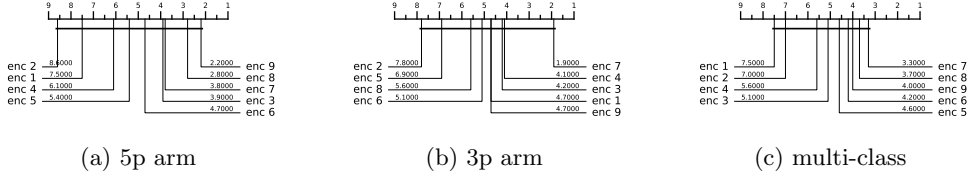


Fig. 8: CD diagrams to compare different encoding methods.

448 3.3 Running time analysis

449 To compare the computational efficiency of MTSCCleav and DiCleave, we conducted a
 450 comparative analysis of their running times. For DiCleave, we employed the code from
 451 its supporting website¹², without any modifications. All experiments were conducted
 452 on the same machine (a personal laptop equipped with an Apple M1 Pro chip and 16
 453 GB of memory) and using the same splits of the training and test datasets under 5-fold
 454 cross-validation to ensure fairness. The reported running times are the averages of the
 455 five runs. The timing results were measured from the training phase to the return of the
 456 five classification metrics. The result is shown in Table 8. MiniROCKET is the most
 457 computationally efficient of the five rocket-based classifiers. We also included its best
 458 result, along with the corresponding encoding method, even though this combination
 459 may not be the best overall.

460 MTSCCleav demonstrated a significant advantage in computational efficiency,
 461 achieving an average 27.0X, 3.7X, and 10.7X speedup over DiCleave, for the 5p arm,
 462 3p arm, and multi-class datasets, respectively. If we consider using the MiniROCKET
 463 in the case of 3p arm and multi-class datasets, it achieves 16.1X and 28.8X speedup.
 464 To note, in the case of the 3p arm dataset, the performance of MiniROCKET is only
 465 slightly lower than DiCleave. In the case of the multi-class dataset, even the perfor-
 466 mance of MiniROCKET is better than DiCleave. DiCleave is a deep learning-based
 467 method that requires substantial time for model inference, while MTSCCleav lever-
 468 ages efficient ROCKET-based classifiers. This significant reduction in runtime makes
 469 MTSCCleav more suitable for large-scale data and real-time applications.

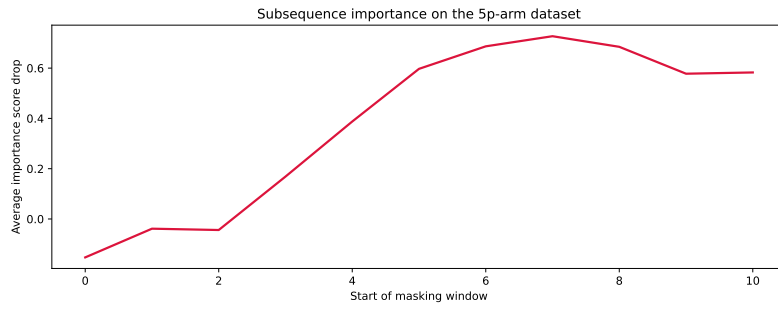
¹²

<https://github.com/MGuard0303/DiCleave> (Accessed on: 2025-07-13).

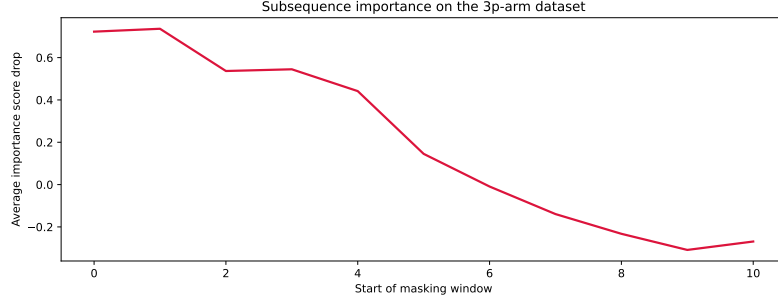
470 3.4 Subsequence importance

471 To evaluate the sensitivity of MTSCCleav to subsequences of the input, we conducted a
 472 perturbation experiment to evaluate the importance of subsequences based on masking
 473 windows. The goal of this experiment is to identify which subsequences of the entire
 474 time series are critical for classification. We examine how various modifications to the
 475 original input impact model performance. It suggests which features are essential for
 476 classification.

477 The model was trained on the original training dataset. For each instance in the
 478 test dataset, we measure its original score and the masked score. We slid a masking
 479 window w with a fixed length over the input time series T . $|w|$ was set to 4. For each
 480 window position $i \in \{1, 2, \dots, |T|-|w|+1\}$, we masked all entries across all the channels
 481 of T within the window. Hence, we removed or hid that portion of information from
 482 the model during inference. The changes in classification performance in terms of
 483 accuracy relative to the unmasked original score of each i are recorded. Intuitively, if
 484 the information of a subsequence is critical for the classification, the masking of this
 485 subsequence would lead to a great drop in classification performance. We aggregated
 the importance score across the test dataset. The result is shown in Figure 9. For the



(a) 5p arm



(b) 3p arm

Fig. 9: Results of the perturbation experiment.

486 encoding methods, we cannot use the methods derived from the cumulative mapping
487 because the accumulation would leak information from the masked region. We adopted
488 “Grouped fixed-length channel mapping” as the encoding method and ROCKET as
489 the classifier. “Grouped fixed-length channel mapping” is the best encoding, other
490 than the methods derived from the cumulative mapping, in all datasets, as shown in
491 Figure 8. ROCKET is the best classifier, as shown in Figure 7..

492 In the 5p arm dataset, we found that masking subsequences at the tailing part
493 caused a significant drop in the importance score, as shown in Figure 9 (a). In the
494 3p arm dataset, we found that masking subsequences at the leading part caused a
495 significant drop in the importance score, as shown in Figure 9 (b).

496 4 Discussion

497 The channel ablation study reveals that the involvement of the time series derived
498 from the secondary structure can improve accuracy. It suggests the importance of
499 RNA folding in dicer processing. Additionally, we found that the base-pair probabil-
500 ity sequence of the secondary structure can also enhance accuracy. To the best of our
501 knowledge, it is a novel application of the base-pair probability sequence. Experiments
502 show that using the probability sequence as an additional channel can enhance accu-
503 racy more than incorporating it in the encoding. It is likely because keeping it as an
504 additional channel can preserve more information, of both the probability sequence
505 itself and the complementary strand.

506 Out of the three datasets, the best classifier is ROCKET. The ranking of the five
507 classifiers by performance, starting from the best, is as follows: ROCKET, Hydra,
508 MiniROCKET, MultiROCKET-Hydra, and MultiROCKET. It indicates that the fea-
509 tures created from the pooling operations that are only in MultiROCKET but not in
510 MiniROCKET, confuse the final classifier. They are mean of positive values (MPV),
511 mean of indices of positive values (MIPV) and longest stretch of positive values
512 (LSPV) [34]. In contrast, the pooling operator that is only present in ROCKET but
513 not in MiniROCKET, enhances the classification performance. It is maximum (MAX).

514 For the encoding methods, we have the following observations. Fixed-length
515 grouped channel mappings outperform variable-length counterparts with one excep-
516 tion in the multi-class dataset, likely because fixed-length schemes better preserve
517 the original positional information of nucleotides within the sequence. Global cumu-
518 lative methods consistently yield better performance than local cumulative methods.
519 It suggests that the upstream information of the cleavage pattern plays a critical role
520 in identifying cleavage sites. Cumulative-based encodings perform better than single-
521 value mappings, with one exception in the 3p dataset, suggesting that the accumulated
522 nucleotide signal is more informative for cleavage site prediction than the local or iso-
523 lated presence of nucleotides. In the 5p arm dataset, encoding RNA sequence in two
524 channels appears to worsen the result. This suggests that the 5p arm dataset and the
525 3p arm dataset need different nucleotide grouping methods for the encoding.

526 One limitation of DiCleave is overfitting during training because of the relatively
527 small size of the dataset [11]. DiCleave is a deep learning-based method. Deep learning
528 models typically require a large amount of training data to generalize effectively. They

529 are data-hungry. In contrast, MTSCCleav leverages ROCKET-based methods for the
530 classification. They rely on random convolutional feature extraction followed by a sim-
531 ple linear classifier. The Ridge classifier used in this study is less data-hungry compared
532 to deep learning methods due to its use of L2 regularization and the simplicity of its
533 linear model nature. It allows ROCKET-based classifiers, and hence MTSCCleav, to
534 maintain strong predictive performance even in settings with a relatively small dataset
535 size.

536 The subsequence importance reveals some connections between RNA secondary
537 structure and human dicer cleavage site prediction. The perturbation experiment
538 shows that the leading part of 5p arm and the tailing part of 3p arm are important
539 for the classification. These parts are close to the center of the RNA secondary struc-
540 ture of pre-miRNA. It indicates that the center region is more crucial for human dicer
541 cleavage site prediction. It agrees with the previous study [10].

542 5 Conclusions

543 We proposed an accurate, fast, and simple multivariate time series classification
544 (MTSC)-based method, termed MTSCCleav, for predicting human dicer cleavage sites.
545 Base-pair probability sequences of the secondary structures have also been leveraged
546 in the classification. MTSCCleav consists of three parts: time series encoding, time
547 series transformation, and classification. ROCKET-based methods were used for time
548 series transformation. Ridge Classifier was used for classification. For the computa-
549 tional experiments, we evaluated nine time series encoding methods in conjunction
550 with five time series transformation methods. MTSCCleav outperformed the SOTA
551 method in all five evaluation metrics for the 5p-arm and multi-class datasets, and four
552 of the metrics for the 3p-arm dataset. In terms of computational efficiency, MTSC-
553 Cleav with the optimal setting achieved an average 3.7X to 27.0X speedup over the
554 SOTA method on the three datasets. With the use of a less accurate but faster time
555 series transformation method, MTSCCleav achieved an average speedup of 16.1X to
556 28.8X, respectively. We analyzed the subsequence importance of the input multivari-
557 ate time series. The results show that subsequences near the center of the pre-miRNA
558 sequences are more important. This aligns with the findings from previous work. This
559 study demonstrates that time series analysis provides a powerful alternative to conven-
560 tional modeling in the context of RNA processing. This framework may be extended to
561 other RNA-processing tasks. Notably, the encoding of RNA sequence into time series
562 enables us to utilize any well-established tools from the time series community.

563 References

- 564 [1] Urry, L.A., Cain, M.L., Wasserman, S.A., Minorsky, P.V., Orr, R.B., Campbell,
565 N.A.: *Campbell Biology*, Twelfth edition edn., New York, NY (2020)
- 566 [2] Alberts, B.: *Molecular Biology of the Cell*, Seventh edition edn., New York (2022)
- 567 [3] Cohen, W.W.: *A Computer Scientist's Guide to Cell Biology: A Travelogue from*
568 *a Stranger in a Strange Land*, New York, NY (2007)

- 569 [4] Lee, Y., Jeon, K., Lee, J.-T., Kim, S., Kim, V.N.: Microrna maturation: Stepwise
 570 processing and subcellular localization. *The EMBO Journal* **21**(17), 4663–4670
 571 (2002)
- 572 [5] Gu, S., Jin, L., Zhang, Y., Huang, Y., Zhang, F., Valdmanis, P.N., Kay, M.A.:
 573 The loop position of shrnas and pre-mirnas is critical for the accuracy of dicer
 574 processing in vivo. *Cell* **151**(4), 900–911 (2012)
- 575 [6] Feng, Y., Zhang, X., Graves, P., Zeng, Y.: A comprehensive analysis of precursor
 576 microrna cleavage by human dicer. *RNA* **18**(11), 2083–2092 (2012)
- 577 [7] MacRae, I.J., Zhou, K., Doudna, J.A.: Structural determinants of rna recognition
 578 and cleavage by dicer. *Nature Structural & Molecular Biology* **14**(10), 934–940
 579 (2007)
- 580 [8] Ahmed, F., Kaundal, R., Raghava, G.P.: Phdcleav: A svm based method for
 581 predicting human dicer cleavage sites using sequence and secondary structure of
 582 mirna precursors. *BMC Bioinformatics* **14**(14), 9 (2013)
- 583 [9] Bao, Y., Hayashida, M., Akutsu, T.: Lbsizecleav: Improved support vector
 584 machine (svm)-based prediction of dicer cleavage sites using loop/bulge length.
 585 *BMC Bioinformatics* **17**(1), 487 (2016)
- 586 [10] Liu, P., Song, J., Lin, C.-Y., Akutsu, T.: Recgbm: A gradient boosting-based
 587 method for predicting human dicer cleavage sites. *BMC Bioinformatics* **22**(1), 63
 588 (2021)
- 589 [11] Mu, L., Song, J., Akutsu, T., Mori, T.: Dicleave: A deep learning model for
 590 predicting human dicer cleavage sites. *BMC Bioinformatics* **25**(1), 13 (2024)
- 591 [12] Mu, L., Akutsu, T.: DiCleavePlus: A Transformer-Based Model to Detect Dicer
 592 Cleavage Sites within Cleavage Patterns. Submitted, under review (2025). <https://github.com/MGuard0303/DiCleavePlus>
- 593 [13] Griffiths-Jones, S., Saini, H.K., van Dongen, S.: mirbase: Tools for microrna
 594 genomics. *Nucleic Acids Research* **36**(suppl_1), 154–158 (2008)
- 595 [14] Xu, T., Su, N., Liu, L., Zhang, J., Wang, H., Zhang, W., Gui, J., Yu, K., Li, J., Le,
 596 T.D.: mirbaseconverter: An r/bioconductor package for converting and retrieving
 597 mirna name, accession, sequence and family information in different versions of
 598 mirbase. *BMC Bioinformatics* **19**(19), 514 (2018)
- 599 [15] Zvelebil, M.J., Baum, J.O., Zvelebil, M.: Understanding Bioinformatics, New York
 600 (2008)
- 601 [16] Lorenz, R., Bernhart, S.H., Höner zu Siederdissen, C., Tafer, H., Flamm, C.,
 602 Stadler, P.F., Hofacker, I.L.: Viennarna package 2.0. Algorithms for Molecular

- 604 Biology **6**(1), 26 (2011)

605 [17] Aggarwal, C.C.: Data Mining: The Textbook, Cham (2015)

606 [18] Mendizabal-Ruiz, G., Román-Godínez, I., Torres-Ramos, S., Salido-Ruiz, R.A.,
607 Morales, J.A.: On dna numerical representations for genomic similarity compu-
608 tation. PLOS ONE **12**(3), 0173288 (2017)

609 [19] Anastassiou, D.: Genomic signal processing. IEEE Signal Processing Magazine
610 **18**(4), 8–20 (2001)

611 [20] Rakthanmanon, T., Campana, B., Mueen, A., Batista, G., Westover, B., Zhu, Q.,
612 Zakaria, J., Keogh, E.: Searching and mining trillions of time series subsequences
613 under dynamic time warping. In: Proceedings of the 18th ACM SIGKDD Interna-
614 tional Conference on Knowledge Discovery and Data Mining. KDD '12, pp.
615 262–270, New York, NY, USA (2012)

616 [21] Cristea, P.D.: Conversion of nucleotides sequences into genomic signals. Journal
617 of Cellular and Molecular Medicine **6**(2), 279–303 (2002)

618 [22] Chakravarthy, N., Spanias, A., Iasemidis, L.D., Tsakalis, K.: Autoregressive mod-
619 eling and feature analysis of dna sequences. EURASIP Journal on Advances in
620 Signal Processing **2004**(1), 1–16 (2004)

621 [23] Zhao, J., Yang, X.W., Li, J.P., Tang, Y.Y.: Dna sequences classification based on
622 wavelet packet analysis. In: Wavelet Analysis and Its Applications, pp. 424–429
623 (2001)

624 [24] Holden, T., Subramaniam, R., Sullivan, R., Cheung, E., Schneider, C., Jr, G.T.,
625 Flamholz, A., Lieberman, D.H., Cheung, T.D.: Atcg nucleotide fluctuation of
626 deinococcus radiodurans radiation genes. In: Instruments, Methods, and Missions
627 for Astrobiology X, vol. 6694, pp. 402–411 (2007)

628 [25] Nair, A.S., Sreenadhan, S.P.: A coding measure scheme employing electron-ion
629 interaction pseudopotential (eiip). Bioinformation **1**(6), 197–202 (2006)

630 [26] Akhtar, M., Epps, J., Ambikairajah, E.: On dna numerical representations
631 for period-3 based exon prediction. In: 2007 IEEE International Workshop on
632 Genomic Signal Processing and Statistics, pp. 1–4 (2007)

633 [27] Zhang, R., Zhang, C.-T.: Z curves, an intutive tool for visualizing and analyzing
634 the dna sequences. Journal of Biomolecular Structure and Dynamics **11**(4), 767–
635 782 (1994)

636 [28] Berger, J.A., Mitra, S.K., Carli, M., Neri, A.: Visualization and analysis of dna
637 sequences using dna walks. Journal of the Franklin Institute **341**(1), 37–53 (2004)

638 [29] Bagnall, A., Lines, J., Bostrom, A., Large, J., Keogh, E.: The great time series

- 639 classification bake off: A review and experimental evaluation of recent algorithmic
640 advances. *Data Mining and Knowledge Discovery* **31**(3), 606–660 (2017)
- 641 [30] Ruiz, A.P., Flynn, M., Large, J., Middlehurst, M., Bagnall, A.: The great multi-
642 variate time series classification bake off: A review and experimental evaluation
643 of recent algorithmic advances. *Data Mining and Knowledge Discovery* **35**(2),
644 401–449 (2021)
- 645 [31] Middlehurst, M., Schäfer, P., Bagnall, A.: Bake off redux: A review and experi-
646 mental evaluation of recent time series classification algorithms. *Data Mining and*
647 *Knowledge Discovery* **38**(4), 1958–2031 (2024)
- 648 [32] Dempster, A., Petitjean, F., Webb, G.I.: Rocket: Exceptionally fast and accurate
649 time series classification using random convolutional kernels. *Data Mining and*
650 *Knowledge Discovery* **34**(5), 1454–1495 (2020)
- 651 [33] Dempster, A., Schmidt, D.F., Webb, G.I.: Minirocket: A very fast (almost) deter-
652 ministic transform for time series classification. In: Proceedings of the 27th ACM
653 SIGKDD Conference on Knowledge Discovery & Data Mining. KDD '21, pp.
654 248–257, New York, NY, USA (2021)
- 655 [34] Tan, C.W., Dempster, A., Bergmeir, C., Webb, G.I.: Multirocket: Multiple pool-
656 ing operators and transformations for fast and effective time series classification.
657 *Data Mining and Knowledge Discovery* **36**(5), 1623–1646 (2022)
- 658 [35] Dempster, A., Schmidt, D.F., Webb, G.I.: Hydra: Competing convolutional ker-
659 nels for fast and accurate time series classification. *Data Mining and Knowledge*
660 *Discovery* **37**(5), 1779–1805 (2023)
- 661 [36] Matthews, B.W.: Comparison of the predicted and observed secondary structure
662 of t4 phage lysozyme. *Biochimica et Biophysica Acta (BBA) - Protein Structure*
663 **405**(2), 442–451 (1975)
- 664 [37] Gorodkin, J.: Comparing two k-category assignments by a k-category correlation
665 coefficient. *Computational Biology and Chemistry* **28**(5), 367–374 (2004)